

Domain Reversal Dynamics in Ferromagnetic Thin Films of Co/Pd Nanomultilayers

Sug-Bong CHOE, Dong-Hyun KIM and Sung-Chul SHIN

*Department of Physics and Center for Nanospinics of Spintronic Materials,
Korea Advanced Institute of Science and Technology, Taejeon 305-701*

(Received 28 December 2001)

Domain reversal dynamics in ferromagnetic thin films has been quantitatively investigated by means of a magneto-optical microscope magnetometer (MOMM), capable of grabbing domain reversal patterns in real time under an applied magnetic field and of measuring local magnetic properties with 400-nm spatial resolution. The domain reversal behavior sensitively changed between wall-motion and nucleation-dominant behavior with changing multilayer structure of the Co/Pd multilayers. Quantitative analysis revealed that the contrasting reversal behavior was mainly caused by a sensitive change in wall-motion speed and that the reversal ratio of wall-motion speed over nucleation rate was a governing parameter for the contrasting domain reversal dynamics. The activation volumes of the wall-motion and nucleation processes were generally unequal, and the inequality was closely related with the domain dynamics. Based on a Monte-Carlo simulation, both the macroscopic magnetic properties and the local magnetic variation were responsible for the contrasting domain reversal behavior.

PACS numbers: 75.60.Ej

I. INTRODUCTION

Domain configurations and reversal dynamics become important subjects in high-density magnetic and magneto-optical recording since they govern the formation of the written domain size, irregularity, and stability [1–7]. To achieve high performance in magnetic information technologies, it is essential to explore the dynamic properties of magnetic materials since information is stored in the form of magnetic domains and the magnetization reversal process of domains under an applied magnetic field is involved. Much effort has been devoted to investigating magnetic domains in a number of systems [8–15] and recently, understanding of domain configurations has progressed greatly, largely motivated by direct observations of domain structures using advanced magnetic imaging techniques with spatial resolutions of some tens of nanometers [16–22]. However, despite the advantage of the high spatial resolution of these imaging techniques, dynamic studies have rarely been carried out due to the limitations imposed by applying a magnetic field and/or slow data acquisition time.

Characterization of magnetic domain dynamics is also important from a fundamental point of view. Interest has rapidly grown due to experimental observation of contrasting magnetization reversal dynamics between the wall-motion dominant and the nucleation-dominant processes exhibited in similar samples of many systems [1–15]. Macroscopic magnetic properties have been ex-

amined to explain the intrinsic origin of the contrasting reversal dynamics based on a micromagnetic consideration of a thermally activated reversal process: it has been well explained that contrasting reversal dynamics may occur among uniform magnetic films of different macroscopic magnetic properties [23–27]. In addition, structural irregularities caused by lattice mismatch [1], interfacial roughness [12, 28], and local structural variation [8, 29] have been conjectured to be another origin of the contrasting reversal dynamics. It is very apparent that domain evolution is microscopically affected by spatial inhomogeneity in magnetic properties, such as coercive forces and magnetization [30–34]. However, fundamental understanding of their influences requires microscopic studies, including measurements of the microstructural (or micromagnetic) properties and real-time observation of the domain evolution structure in a magnetic field, where both experiments need to be carried out on identical microscopic areas of a sample. The first quantitative results of such correlations were reported very recently [32–34].

In this article, we have investigated the magnetization reversal dynamics of ferromagnetic Co/Pd multilayer films and the origin of its contrasting magnetization reversal behavior. For this study, we have developed a magneto-optical microscope magnetometer (MOMM) capable of grabbing domain reversal patterns in real time under an applied magnetic field, and of simultaneously probing local magnetic properties with a 400-nm spatial

resolution. Using the MOMM system, we have investigated domain reversal dynamics in Co/Pd multilayers. Wall-motion speed and nucleation rate have been quantitatively determined based on time-resolved domain evolution patterns. From the field dependence of the wall-motion speed and nucleation rate, we have measured activation volumes of the wall-motion and nucleation processes within the context of a thermally activated relaxation process. To understand the experimental finding, we studied domain reversal dynamics theoretically by using a Monte-Carlo simulation. This paper is organized as follows: We present the experimental procedure in Sec. II, the sample preparation in Sec. III, the experimental observation of the domain reversal dynamics in Sec. IV, the quantitative analysis on the domain reversal dynamics in Sec. V, the determination of the activation volumes in Sec. VI, the discussion on the origins of the contrasting domain reversal dynamics in Sec. VII, and the summary of our findings in Sec. VIII.

II. TECHNICAL OUTLINE

The MOMM system is a magnetometric setup of a magneto-optical Kerr microscope, which is basically an polarizing optical microscope capable of detecting magnetic contrast via the magneto-optical Kerr effect [32–34]. The microscope can visualize the perpendicular component of the magnetization via the polar Kerr effect with a normal incidence of illuminating light or the longitudinal component of the magnetization via the longitudinal Kerr effect with a inclined incidence of illuminating light by shifting the objective lens and adjusting the relevant optical components.

The maximum spatial resolution of our optical microscope (Olympus, BX-60M) is about 400 nm at the maximum 1,000 \times magnification when using a 100-W mercury illumination lamp. The mercury lamp is powered via an automatic voltage regulator to enhance the stability. If a sheet-type polarizer/analyzer and stress-free polarizing objective lens are adopted, the Kerr angle resolution in the polar geometry (or bright field illumination) is less than 0.2° for a fast dynamic measurement and 0.01° for a slow quasi-static measurement.

The system is equipped with an electromagnet controlled by a personal computer to apply an external magnetic field to a sample in the range of ± 3.5 kOe with a field resolution of less than a few tens of Oe. The field rising rate is about 10^{-4} s/Oe with low-pass filter electronic circuit, and we control the electromagnet to be slower than the field rising rate to avoid an overshoot problem. The electromagnet is positioned just below the sample stage with a gap of about 2 mm. The applied magnetic field from the 6-mm-diameter magnetic pole tip is thought to be uniform at a sample over a field of view about 100 μ m in diameter. The electromagnet is cooled with water to avoid temperature changes in a sample

as well as thermal drift effects on the sample stage. To enhance the stage stability, we remove all magnetic materials, as well as all rubbers, from the micropositioner of the stage. The stage usually goes to a stable position within an hour after sample positioning, then, it remains stable over a few hours, which is enough to carry out an experiment.

An advanced charge-coupled device (CCD) camera system equipped with a signal intensifier is attached to the microscope to store the magnetic images into a computer with a video rate. The signal intensifier of multi-channel plates intensifies the image intensity up to 10^4 times to visualize the detailed contrast change from a small Kerr rotation angle usually less than 0.1°. The physical size of a unit CCD pixel is adjusted to correspond to an area of 200×200 nm² at the film surface, and we use the sum of a 2×2 pixel array as a logical pixel size Δ to meet the spatial resolution of the microscope; this logical definition of a pixel size will be used from now on. In the current setup, a domain image is composed of 100×80 logical CCD pixels. The domain image is then given by an array of the Kerr intensity $I(x, y)$ measured by each position-specified (x, y) th CCD pixel, where x and y are integers.

By storing domain images $I(x, y)$ while sweeping the external magnetic field h , one obtains a three-dimensional array of the Kerr intensity $I(x, y; h)$, as depicted in Fig. 1(a), where each pixel contains the position- and field-specified element of the measured Kerr intensity. The cross-sectional mapping onto the (x, y) plane gives the conventional domain images $I_h(x, y)$ at a given field h , as shown in Fig. 1(b). However, we would like to point out that tracing along a (x, y) pixel provides a Kerr intensity variation $I_{xy}(h)$ with respect to sweeping an applied field h , as shown in Fig. 1(c). The Kerr intensity variation $I_{xy}(h)$ directly correlates to the magnetic hysteresis loop from a local region of Δ^2 area at the (x, y) th position [32].

Figure 2(a) shows a typical Kerr intensity variation $I_{xy}(h)$. The intensity $I_{xy}(h)$ is correlated with the Kerr rotational angle $\theta_{xy}(h)$ as

$$I_{xy}(h) = I_{xy}^{(0)} + C_{xy} \sin^2 [\theta_{xy}(h) + \alpha_{xy} h + \delta\theta_{xy}], \quad (1)$$

where $I_{xy}^{(0)}$ is the intensity offset of the corresponding CCD pixel, C_{xy} is the proportionality coefficient between the intensity and the Kerr rotational angle, α_{xy} is the Faraday coefficient incurred at the objective lens of the microscope, and $\delta\theta_{xy}$ is the angle between the polarizer and the analyzer [32]. Fitting the measured $I_{xy}(h)$ versus h with Eq. (1) for the two saturated states of $\theta_{xy}(h) = \pm\theta_{xy}^{(M)}$, as shown by the solid lines in Fig. 2(a), one can determine the values of $I_{xy}^{(0)}$, $C_{xy}\alpha_{xy}^2$, $\delta\theta_{xy}/\alpha$, and $\theta_{xy}^{(M)}/\alpha$ under an approximation of $\sin\theta \sim \theta$ for a small θ . Then, the normalized Kerr hysteresis loop can be generated from the intensity variation with the fitting quantities

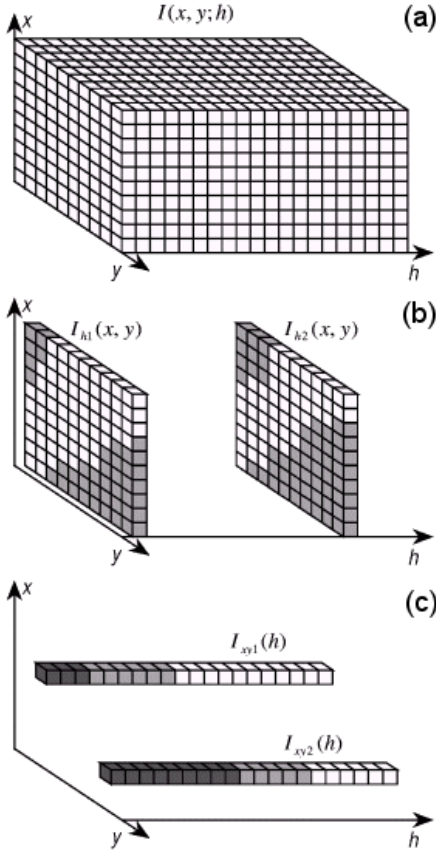


Fig. 1. (a) Schematic drawing of a three-dimensional array of the position- and field-specified Kerr intensity. (b) Conventional field-dependent domain images, as cross-sectional views of the three-dimensional array. (c) Field-dependent Kerr intensity variation, tracing along a CCD pixel at a fixed position.

and is given by

$$\frac{\theta_{xy}(h)}{\theta_{xy}^{(M)}} = \frac{\alpha_{xy}}{\theta_{xy}^{(M)}} \left(\sqrt{\frac{I_{xy}(h) - I_{xy}^{(0)}}{C_{xy}\alpha_{xy}^2}} - h \right) - \frac{\delta\theta_{xy}}{\theta_{xy}^{(M)}}. \quad (2)$$

Figure 2(b) shows the normalized Kerr hysteresis loop generated from the intensity variation shown in Fig. 2(a). It was confirmed that the measured hysteresis loop of a given local area was basically identical for several different runs. Note that this Kerr hysteresis loop generation process can be simultaneously carried out for every CCD pixel once a three-dimensional array of field-dependent domain images is provided. Thus, from the position-specified array of the local hysteresis loops, one generates a two-dimensional distribution map of the local coercivity $H_C(x, y)$.

A similar measurement technique can be applied to measure the local magnetization viscosity curves [33]. In this experiment, a sample is first saturated by applying a magnetic field normal to the film plane; then, magnetization reversal is triggered by applying a constant mag-

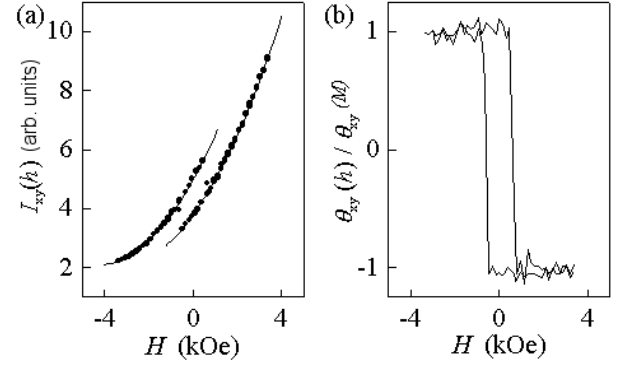


Fig. 2. (a) Typical value of the local intensity variation $I_{xy}(h)$ measured by using the (x, y) th CCD pixel as a function of the applied magnetic field H . The solid lines are the fitting curves given by Eq. (1) for the two saturated states of $\theta_{xy}(h) = \pm\theta_{xy}^{(M)}$. (b) The normalized Kerr hysteresis loop $\theta_{xy}(h)$ generated from the intensity variation shown in (a).

netic field h . From the experiment, a three-dimensional array $I(x, y; t)$ is obtained by storing the time-resolved domain images $I(x, y)$ with respect to the elapsed time t during magnetization reversal. Tracing a (x, y) pixel provides the local magnetization viscosity curve $I_{xy}(t)$, as shown in Fig. 3(a); then, one can determine the local magnetization switching time $\tau(x, y)$, where τ is the time needed to reverse a half of the corresponding local area under a given reversing field. From the position-specified array of the local switching time $\tau(x, y)$, one generates a two-dimensional distribution map of the local switching time. On the other hand, repeating the $\tau(x, y)$ measurement while changing the applied field h , as shown in Fig. 3(b), one can obtain another three-dimensional array of field-dependent $\tau(x, y; h)$, which provides the distribu-

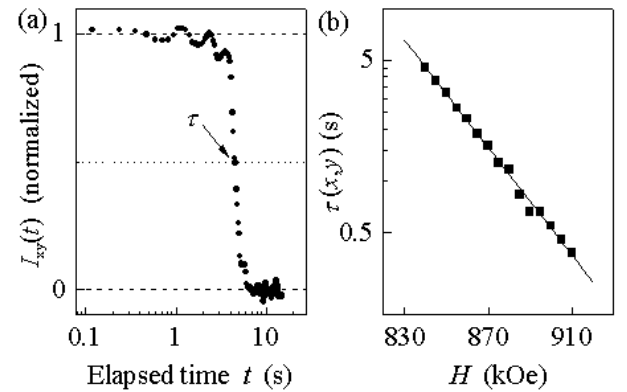


Fig. 3. (a) Typical viscosity curve measured from a CCD pixel corresponding to an area of $0.4 \times 0.4 \mu\text{m}^2$ at the $(2.5\text{-\AA} \text{ Co}/11\text{-\AA} \text{ Pd})_{10}$ sample surface. The y -axis was normalized between the Kerr signals from the initially saturated state and the completely reversed state. (b) Field dependence of the magnetization switching time of the given local area. The solid line is the best fit using Eq. (14).

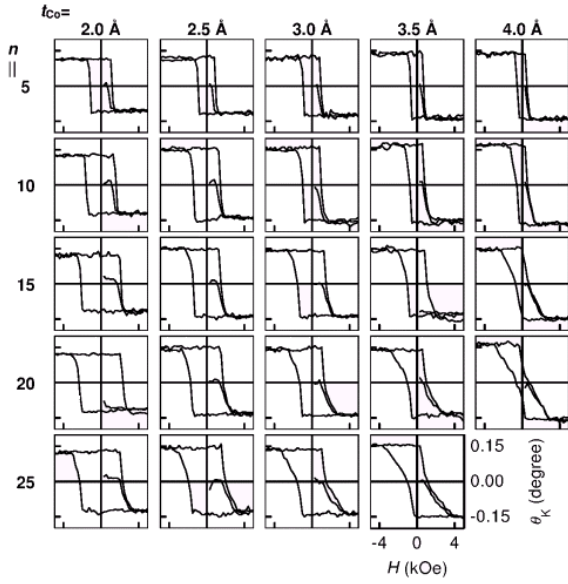


Fig. 4. Polar Kerr hysteresis loops of the $(t_{Co}\text{-Co}/11\text{-}\text{\AA}\text{ Pd})_n$ samples. Each box is aligned in a column with t_{Co} and in a row with n , where the y -axis is the Kerr rotational angle and the x -axis is the applied field.

tion map of the activation magnetic moment $m_A(x, y)$, as will be discussed in Sec. VII.

This simultaneous measurement scheme enables us to avoid measurement errors from different runs, as well as magnetic aftereffects due to a long measurement time. In addition, the most striking feature of the present system is the fact that one can directly map the local distribution of magnetic properties at precisely the same position of a sample. Therefore, the local variations of the magnetic properties can be directly compared with each other to search for any possible correlations between them. The ability of spatially-resolved probing of magnetic properties enables us not only to determine their real distributions but also to obtain in-depth understanding of domain reversal dynamics.

III. SAMPLE PREPARATION

For the purpose of our study, Co/Pd multilayer thin films were chosen based on the following rationale [5, 32–35]. Because of the multilayer structure, one can investigate a variety of samples having different magnetic and/or structural properties by varying the thickness of the ferromagnetic Co layer and the number of repeats. Additionally, it is relatively easy to capture fine domain images when using a magneto-optical Kerr effect (MOKE) microscope since a large polar Kerr effect exists in this material. A number of $(t_{Co}\text{-Co}/11\text{-}\text{\AA}\text{ Pd})_n$ samples with various Co-sublayer thicknesses t_{Co} or the numbers of repeats n were prepared on glass substrates by alternatively exposing two e-beam sources of

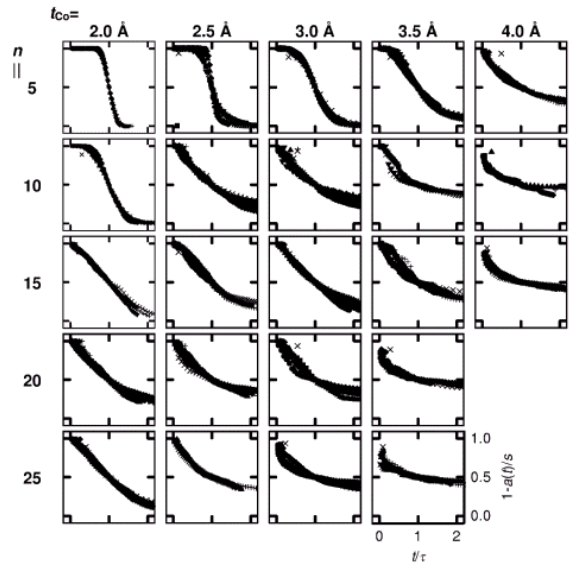


Fig. 5. Magnetization viscosity curves of the $(t_{Co}\text{-Co}/11\text{-}\text{\AA}\text{ Pd})_n$ samples. Each box is aligned in a column with t_{Co} and in a row with n , where the y -axis is the Kerr rotational angle and the x -axis is the applied field.

Co and Pd under a base pressure of 2.0×10^{-7} Torr at ambient temperature [5]. The layer thickness was carefully controlled within a 4% accuracy. Low-angle X-ray diffraction studies using Cu $K\alpha$ radiation revealed that all samples had distinct peaks, indicating the existence of the multilayer structure. High-angle X-ray diffraction studies showed that the samples grew along the [111] cubic orientation. Figure 4 shows the polar Kerr hysteresis loops of all the $(t_{Co}\text{-Co}/11\text{-}\text{\AA}\text{ Pd})_n$ samples in this study. All samples in this study had perpendicular magnetic anisotropy and showed square Kerr hysteresis loops. The maximum Kerr rotational angle increased with increasing t_{Co} while it remained unchanged with increasing n . The coercivity decreased with increasing t_{Co} while it increased with increasing n . The loops became slanted both with increasing t_{Co} and n . The systematic trend in the hysteresis loops with changing multilayer structure provided direct evidence of the good quality of the samples in this study.

IV. MAGNETIZATION VISCOSITY CURVES

Interestingly enough, reversal phenomena in this system were found to be very sensitively changed from wall-motion dominant reversal to nucleation-dominant reversal with either increasing Co-sublayer thickness from 2 Å to 4 Å or increasing number of repeats n from 5 to 25. In Fig. 5, we show the normalized time-dependent magnetization viscosity curves measured for the $(t_{Co}\text{-Co}/11\text{-}\text{\AA}\text{ Pd})_n$ samples. The viscosity curves were obtained by measuring the temporal variation of the Kerr intensity

under several reversing fields as denoted by different symbols. The Kerr angle and the time in the figure were normalized to the maximum Kerr intensity and to the half relaxation time (or switching time) τ , respectively. The rate of relaxation sensitively depended on the strength of the applied field, but the basic shape of the normalized curves for a given sample remained the same, irrespective of the applied field. One can notice that all the curves could be gathered into a unique curve, irrespective of the strength of the reversing field. This was a general feature of all the samples in this study; thus, the normalized curve could be regarded as the characteristic universal curve representing the magnetization reversal of the sample [34].

The (2-Å Co/11-Å Pd)₅ sample initially exhibits a convex curve, indicating a slow relaxation rate. Then, it shows a more rapid relaxation with time and gradually approaches the complete reversal state. This shape of the curve is known to be the typical shape of thermally activated relaxation with low nucleation probability and fast domain-wall motion [36,37]. In this case, the initial relaxation rate is limited by the probability of nucleation while the intermediate relaxation rate is governed by the successive domain-wall expansion [8]. The final equilibrium state is determined by a counterbalance of the applied field and the demagnetizing field, so every curve reaches a saturation value due to the weak demagnetizing field in the sample.

In contrast, the (4-Å Co/11-Å Pd)₁₀ and (4-Å Co/11-Å Pd)₁₀ samples initially exhibit a concave curve, representing the fast decay rate, and slowly approaches an equilibrium state. This shape can be interpreted as manifesting the typical behavior of a thermally activated relaxation with large nucleation probability and slow domain-wall motion [36,37]. It should be pointed out that due to the strong demagnetizing field in the samples, the degree of magnetization reversal depends on the applied field, and complete reversal is never achieved at small applied fields, even after a long time, as seen in the figure. Though the viscosity measurement revealed a nucleation-dominant reversal, the direct domain observation of the (4-Å Co/11-Å Pd)₁₀ sample did not apparently show truly nucleation-dominant patterns, but dendritic-growth ones. The dendritic growth evolved by means of abrupt jutting-out sprouts, which might be interpreted as a new upcoming nucleation adjacent to existing domain boundary rather than as a domain-wall growth along the dendritic stripe patterns.

The intermediate samples show a good trend between wall-motion dominant and nucleation-dominant behaviors both with changing t_{Co} and n . One might interpret the smooth transition feature as reflecting a thermally activated reversal behavior mixed with a counterbalance between the nucleation and wall-motion mechanisms.

V. DOMAIN REVERSAL DYNAMICS

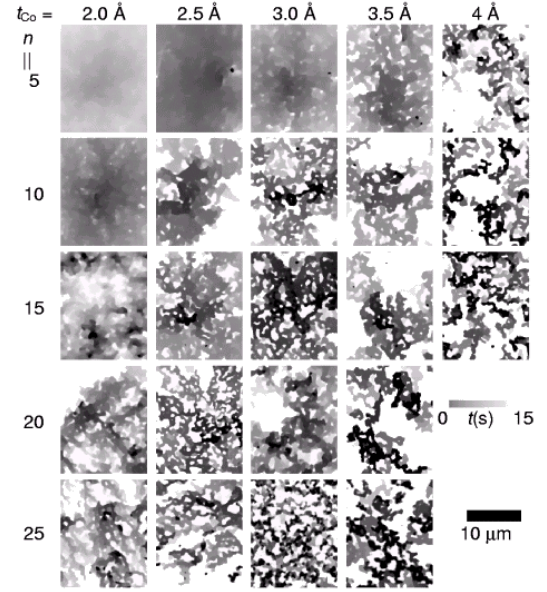


Fig. 6. Typical magnetic domain evolution pattern of the $(t_{Co}\text{-Co}/11\text{-Å Pd})_n$ samples. Each box is aligned in a column with t_{Co} and in a row with n , where the y -axis is the Kerr rotational angle and the x -axis is the applied field. The gray-color filled-in images correspond to the local switching time of the corresponding regions as given by the palette at the bottom right corner.

Contrasting magnetization reversal behaviors were again confirmed by using time-resolved domain observations. Domain reversal behavior has been found to change contrastingly from wall-motion dominant to nucleation-dominant behavior either with increasing Co-sublayer thickness t_{Co} or with increasing number of repeats n . In Fig. 6, we show typical domain reversal patterns of the $(t_{Co}\text{-Co}/11\text{-Å Pd})_n$ samples during domain reversal under a reversed applied field. The gray-color filled-in images correspond to the local switching time as given by the palette at the bottom right corner. It is quite interesting to note that the domain reversal pattern in these serial samples shows a quite contrasting behavior: Wall-motion dominant reversal is vividly seen by a continuous change in the gray level, as shown in the (2.0-Å Co/11-Å Pd)₅ sample, while nucleation-dominant reversal is clearly observed by a discontinuous change in the gray level, as shown in the (4.0-Å Co/11-Å Pd)₅ and the (2.0-Å Co/11-Å Pd)₂₅ samples. All samples show a gradual variation in domain reversal pattern, even with either a 0.5-Å increment in the Co-sublayer or a 5-repeat increment in the number of repeats [5].

1. Quantitative Analysis

To better understand the contrasting reversal behaviors of those samples, we determined the wall-motion speed and the nucleation rate of each sample by using

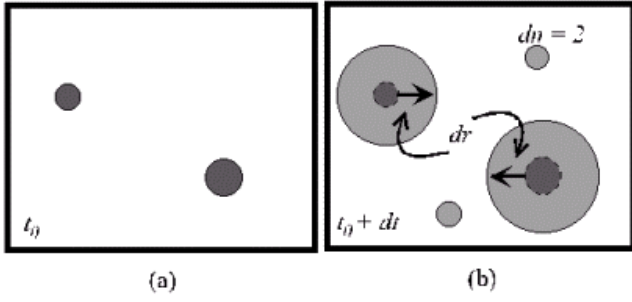


Fig. 7. Schematic illustration of the time-dependent circular domain patterns of magnetization reversal. As time passes from t_0 to $t_0 + dt$, the existing domains expand by dr due to the wall-motion process, and new domains of number dn are nucleated by the nucleation process.

the quantitative analysis technique recently developed by Choe and Shin based on the time-dependent domain reversal patterns. Details of the model have been described elsewhere [7]. Briefly, the model of magnetization reversal is proposed by using the time-dependent domain patterns based on circular domains. In the model, the reversed domains expand at all domain boundaries due to the wall-motion speed V , and simultaneously, new domains are formed at the nucleation rate R per unit time and unit area during magnetization reversal from an initially saturated state. Figure 7 illustrates the time-dependent domain-evolution patterns from an initially saturated state under a reversing applied field. Nucleated domains in Fig. 7(a) expand at all domain boundary due to the wall-motion process, and simultaneously, newly-upcoming domains are formed by the nucleation process, as shown in Fig. 7(b). The expansion of a circular domain, dr , in time dt due to the wall-motion process is given by

$$dr = Vdt, \quad (3)$$

while the number of nucleations, dn , in time dt is given by

$$dn = R(s - a)dt, \quad (4)$$

where V is the wall-motion speed, R is the nucleation probability per unit time and unit area, s is the total area of the sample under examination, and a is the reversed domain area. Since both the wall-motion and the nucleation processes are known to be governed by the thermally activated relaxation mechanism [1,34], the wall-motion speed V and the nucleation probability R are expected to be proportional to $\exp(-E_B(H)/k_B T)$, where $E_B(H)$, which depends on the strength of the reversing field H , is the energy barrier for each process, k_B is the Boltzmann constant, and T is the temperature. Thus, V and R are constant during an isothermal process under a constant reversing field.

Now, the expansion of the reversed domain area, da , is given by

$$da = ldr + \pi r_0^2 dn, \quad (5)$$

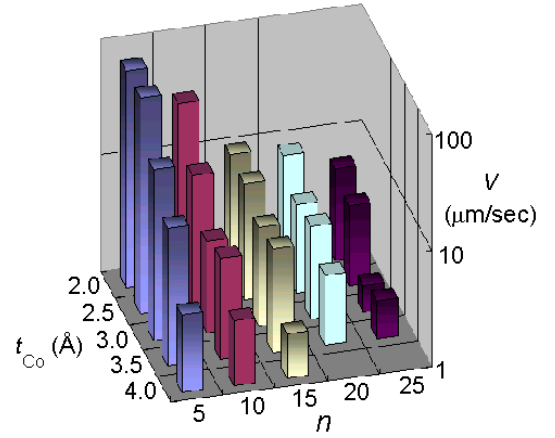


Fig. 8. Wall-motion speed V of the $(t_{Co}\text{-Co}/11\text{-\AA Pd})_n$ samples, where the z -axis is on a logarithmic scale.

where the first term is caused by the wall-motion process at all domain boundaries of length l , and the second one is caused by the nucleation of circular domains having a characteristic radius r_0 . On the other hand, the increment of the domain boundary length dl is given by

$$dl = 2\pi dr + 2\pi r_0 dn. \quad (6)$$

After substituting for dr and dn using Eqs. (3) and (4), Eqs. (5) and (6) become

$$\left. \begin{aligned} a' &\equiv (da/dt) = lV + \pi r_0^2 (s - a)R \\ l' &\equiv (dl/dt) = 2\pi V + 2\pi r_0 (s - a)R \end{aligned} \right\}. \quad (7)$$

Then, the wall-motion speed V and the nucleation probability R are explicitly given by

$$\left. \begin{aligned} V &= (a' - r_0 l' / 2) / (l - \pi r_0) \\ R &= (l l' / 2\pi - a') / (l - \pi r_0) r_0 (s - a) \end{aligned} \right\}. \quad (8)$$

Thus, by measuring the reversed domain area $a(t)$ and the domain boundary length $l(t)$ from the time-resolved serial domain patterns, one can explicitly determine the wall-motion speed V and the nucleation probability R .

The wall-motion speed V and the nucleation rate R of the Co/Pd multilayer samples were determined by using the present method. All the experiments were carried out under a condition of $\tau = 10$ s to avoid errors from different reversal speeds between samples. The wall-motion speed sensitively decreased with either increasing Co-sublayer thickness or increasing number of repeats, as shown in Fig. 8 while the nucleation speed is insensitive to the multilayer structure, as shown in Fig. 9. Thus, one might conclude that the contrasting reversal behavior in this system is caused by a sensitive change in the wall-motion speed.

Based on the values of the wall-motion speed V and the nucleation rate R , we found the reversal ratio V/R to be a governing parameter for contrasting domain reversal dynamics [7] because the reversal behavior is determined by a counterbalance between the wall-motion process

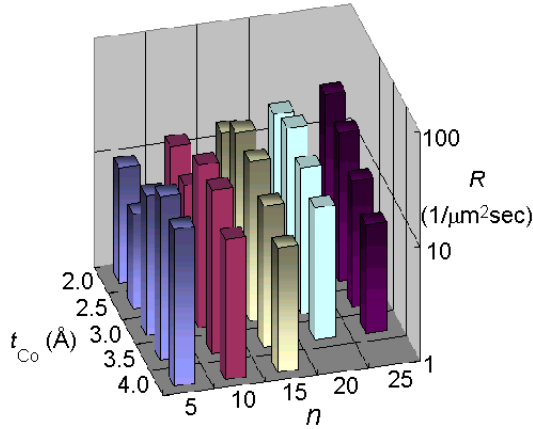


Fig. 9. Nucleation rate per unit area R of the $(t_{\text{Co}}\text{-Co}/11\text{-}\text{Å Pd})_n$ samples, where the z -axis is on a logarithmic scale.

and the nucleation process and because the change in the wall-motion speed among the samples is much larger than the change in the nucleation rate. In Fig. 10, we show the values of the reversal ratio. The reversal ratio sensitively decreases with either increasing Co-sublayer thickness or increasing number of repeats. By comparison of this plot with the domain reversal patterns shown in Fig. 6, we notice that the reversal ratio V/R is an important parameter for characterizing different spin reversal processes: a larger value of V/R yields a more wall-motion dominant process while a smaller value of V/R yields a more nucleation-dominant process. It should be pointed out that even though the wall-motion speed and the nucleation rate are very sensitive to the strength of the applied field, the reversal ratio is quite independent of the applied field.

2. Unequal Activation Volumes

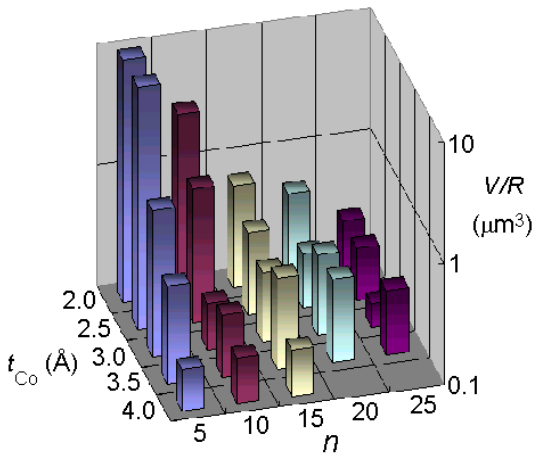


Fig. 10. Reversal ratio V/R of the $(t_{\text{Co}}\text{-Co}/11\text{-}\text{Å Pd})_n$ samples, where the z -axis is on a logarithmic scale.

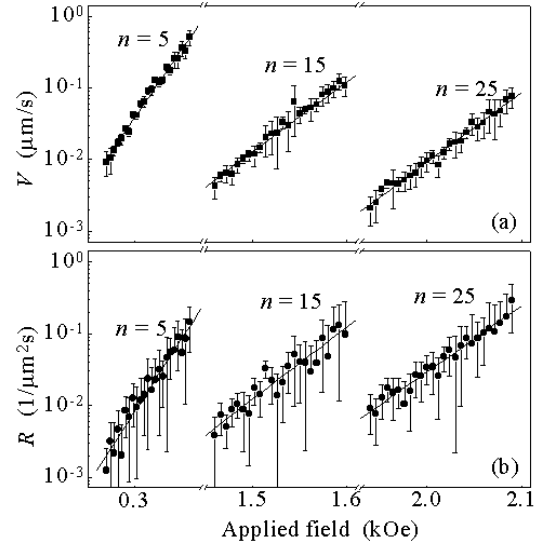


Fig. 11. Dependence of (a) the wall-motion speed V and (b) the nucleation rate R as functions of the reversing applied field for $(2\text{-}\text{Å Co}/11\text{-}\text{Å Pd})_n$ samples with the number of repeats being $n = 5, 15,$ and 25 .

The activation volume, characterizing the unit volume acting as a single-domain particle as well as limiting the minimum sizes of the domains, is a crucial parameter in both the wall-motion and nucleation processes [38, 39]. The wall-motion process takes place either by a successive switching of activation volumes adjacent to existing domains via the thermal activation energy overcoming the finite wall-pinning energy when the applied field is smaller than the wall-pinning field of a film or by a viscous wall-motion process when the applied field is higher than the wall-pinning field of the film [4]. On the other hand, the nucleation process occurs due to random switching of activation volumes at random places via thermal activation energy overcoming the energy barrier of nucleation.

To determine the activation volumes, we have determined the wall-motion speed V and the nucleation rate R of the Co/Pd multilayers from the time-resolved domain patterns during magnetization reversal under various applied fields [34]. In Fig. 11, we plot (a) the wall-motion speed and (b) the nucleation rate of the $(2\text{-}\text{Å Co}/11\text{-}\text{Å Pd})_n$ samples having the $n = 5, 15,$ and 25 number of repeats with respect to the reversing applied field H . Note that the wall-motion speed is very well defined, as seen in Fig. 11(a) while the nucleation rate is rather diffuse, as seen in Fig. 11(b). This is quite expected because the wall motion is a successive process at every domain boundary while the nucleation is a random process statistically governed by the switching probability. It has been found that both reversal parameters exponentially depend on the strength of the reversing applied field. The exponential dependency is strong evidence that both reversal processes are governed by thermally activated relaxation in the range of the reversing applied

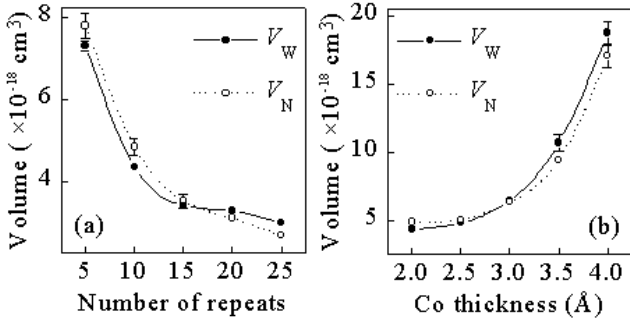


Fig. 12. Wall-motion activation volume V_W and nucleation activation volume V_N of (a) the $(2\text{-}\text{\AA}\text{ Co}/11\text{-}\text{\AA}\text{ Pd})_n$ samples with respect to the number of repeats n and (b) the $(t_{Co}\text{-Co}/11\text{-}\text{\AA}\text{ Pd})_{10}$ samples with respect to the Co-sublayer thickness t_{Co} . The lines are guides for eye, and the error bars indicate the chi-square values of linear fitting.

field in this study. Thus, the dependences should be well fitted by the fitting functions $\log V(\text{or } R) = \alpha + \beta H$. The fitting parameter β corresponds to the magnetic properties, and $\beta = V_A M_S / k_B T$ based on a thermally activated relaxation process [34]. Then, the activation volume V_A can be determined from the field dependency. In Fig. 12, we plot the activation volumes of the wall-motion and the nucleation processes. It is interesting to note that both the activation volumes of the wall-motion and the nucleation processes change in the same way with changing multilayered structure, which implies that both processes are influenced in the same manner by the structural and/or magnetic properties.

Most interestingly, the activation volumes of the wall-motion and the nucleation processes are noticeably different from each other, and the difference between the activation volumes systematically changes in accordance with the variation of the multilayered structure [34]. We find that the difference in the activation volumes is closely related with contrasting domain reversal dynamics. In Fig. 13, we plot the reversal ratio V/R versus the activation volume ratio V_W/V_N , and see a clear correlation between the two ratios, which is evidence for the activation volume ratio being closely related to the magnetization reversal modes. Wall-motion dominant reversal appears when the wall-motion activation volume is smaller than the nucleation activation volume while the nucleation-dominant reversal is observed otherwise because a smaller activation volume results in an easier reversal than a larger one since the activation energy is proportional to the activation volume.

VI. PHASE DIAGRAM

For the contrasting domain reversal behavior, a micromagnetic model has been developed to predict the magnetization reversal dynamics by adopting a Monte

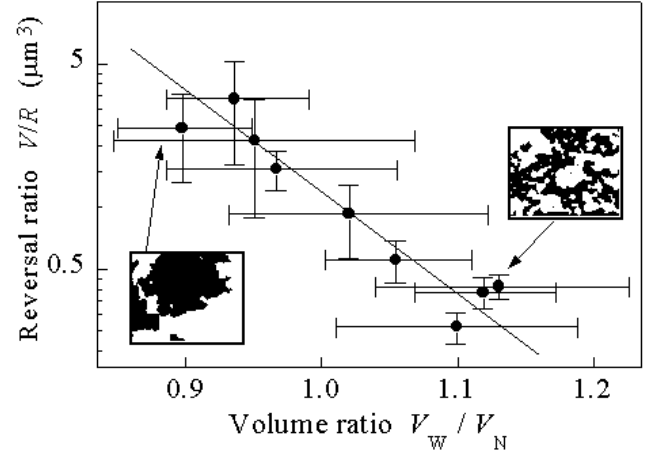


Fig. 13. Correlation between the reversal ratio of the wall-motion speed V over the nucleation rate R and the volume ratio of the wall-motion activation volume V_W over the nucleation activation volume V_N . The domain images in the insets illustrate the typical domain reversal patterns of a wall-motion dominant process for a large V/R and a nucleation-dominant one for a small V/R .

Carlo algorithm based on the uniaxial anisotropy model originally proposed by Kirby *et al.* [5, 24, 27]. In this model, a film is composed of nano-sized identical single-domain cells on hexagonal lattices lying in the XY plane with periodic boundary conditions, as depicted in Fig. 14, and the magnetization of each cell is aligned along the $\pm z$ direction except during the reversal process. Each cell of volume V_c has the saturation magnetization M_s and the uniaxial perpendicular magnetic anisotropy K_u , and each cell boundary has the wall energy density σ_w . Then, the magnetic energy E of a cell with the angle of magnetization direction θ from the $+z$ axis is given by

$$E = K_u V_c \sin^2 \theta - M_s V_c (H + \hat{H}) \cos \theta + 2(1 - \zeta \cos \theta) V_c \sigma_w / d_c \quad (9)$$

where H and \hat{H} are the external magnetic field and the demagnetizing field along the $+z$ direction, respectively. The $\zeta = \sum_k \cos \theta_k / 6$ is the fraction of the magnetization state summed over the nearest-neighboring cells k , and d_c is the distance between the centers of the nearest-neighboring cells. The magnetic energy can be rewritten

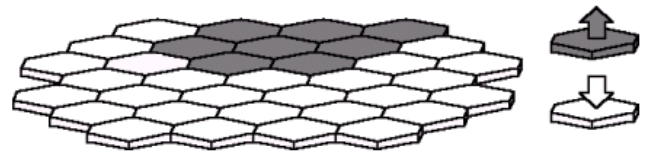


Fig. 14. Unit cells lying on a hexagonal lattice in the XY plane used in the simulation. The magnetization of each cell is aligned along the $\pm z$ direction, except during the reversal process.

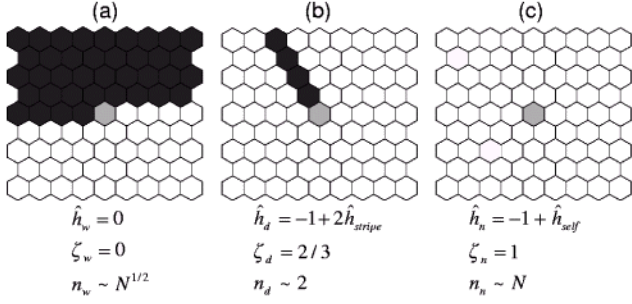


Fig. 15. Typical situations of (a) the wall-motion process, (b) the dendritic-growth process, and (c) the nucleation process. The magnetization reversal situation parameters, \hat{h} , ζ , and n , for the corresponding magnetization reversal situation are given at the bottom of each case. Here, \hat{h}_{stripe} is the contribution to the demagnetizing energy from the cells lying on the linear stripe domain shown as the black cells in (b), and \hat{h}_{self} is the self-demagnetizing energy of a cell.

in a simplified form expressed by

$$E = K_u V_c \left[\sin^2 \theta - 2 \left(\alpha + m \hat{h} + \zeta w \right) \cos \theta + 2w \right] \quad (10)$$

by introducing dimensionless parameters: $m = 2\pi M_s^2 / K_u$ is the ratio of the magnetostatic energy to the anisotropy energy; $w = \sigma_w / t_c K_u$ is the ratio of the wall energy to the anisotropy energy; $\alpha = M_s H / 2K_u$ is the ratio of the applied magnetic field to the anisotropy field; $\hat{h} = \hat{H} / 4\pi M_s$ is the ratio of the demagnetizing field to its maximum value.

The magnetic energy E has two minima, one at $\theta = 0$ and the other at π , with a maximum in between. The energy barrier E_b for reversal is then given by the difference in energy between the initial value and the maximum:

$$E_b = K_u V_c \left[1 + \hat{m} \left(\alpha + m \hat{h} + \zeta w \right) \right]^2, \quad (11)$$

where $\hat{m} = \cos \theta_0$ is the directional cosine of the initial magnetization direction θ_0 of the cell. In a thermally activated magnetization reversal process, magnetization reversal of a cell takes place by overcoming the energy barrier E_b via activation with the thermal energy $k_B T$, and the switching probability of a cell in time Δt is given by

$$p = r_0 \exp \left(-\beta' \left[1 + \hat{m} \left(\alpha + m \hat{h} + \zeta w \right) \right]^2 \right) \Delta t, \quad (12)$$

where r_0 is the probability constant (or inverse of the attempt frequency). Here, $\beta' = K_u V_c / k_B T$ is another dimensionless parameter giving the ratio of the magnetic anisotropy energy of a cell to the thermal activation energy.

The switching probability p of an individual cell is determined according to the magnetization state of the neighboring cells. Now, we consider the typical situations of the three fundamental magnetization reversal

processes illustrated in Fig. 15(a) the wall-motion process takes place by switching a cell at the boundary of an existing domain; (b) the dendritic-growth process switches a cell at the end of a stripe domain; and (c) the nucleation process makes an isolated cell. From the typical situations, one can determine the situation parameters, *i.e.*, the normalized demagnetizing field \hat{h} and the domain-wall coverage ζ for the corresponding magnetization reversal process. The values of the situation parameters are given at the bottom of each illustration. The number of cells, n , under each typical situation was chosen as an approximate quantity.

The probability P_i , where the magnetization reversal process i takes place among all simulation cells, is given by the sum of the individual switching probabilities p_i of the number of cells n_i under a typical situation of the magnetization reversal process i , *i.e.*, $P_i \sim n_i p_i$. The equilibrium condition between the magnetization reversal processes i and j is then given by $P_i = P_j$ since the subsequent magnetization reversal is chosen by the counterbalance between the probabilities of the magnetization reversal processes. Using Eq. (12), the equilibrium condition can be rewritten by using a functional relation between the normalized domain-wall energy w and the normalized magnetostatic energy m :

$$w(m) = \frac{-b_{ij} + \sqrt{b_{ij}^2 - a_{ij} c_{ij}}}{a_{ij}}, \quad (13)$$

where the coefficients a , b , and c are

$$\begin{aligned} a_{ij} &= \zeta_i^2 - \zeta_j^2, \\ b_{ij} &= \left(\hat{h}_i \zeta_i - \hat{h}_j \zeta_j \right) m + (1 + \alpha) (\zeta_i - \zeta_j), \\ c_{ij} &= \left(\hat{h}_i^2 - \hat{h}_j^2 \right) m^2 + 2(1 + \alpha) \left(\hat{h}_i - \hat{h}_j \right) m \\ &\quad - \frac{1}{\beta'} \log \frac{n_i}{n_j}. \end{aligned}$$

Figure 16 illustrates the simulated domain evolution patterns with respect to m and w together, where each frame is aligned in a column with different m and in a row with different w . The w and the m are chosen as the major quantities due to the fact that they directly reflect the effect of the different magnetization reversal situations on the reversal probability via the term $m \hat{h} + \zeta w$ in Eq. (12) whereas the other parameters, such as α , β' , and N , just give the same contribution to all reversal probabilities; the parameters are fixed to $\beta' = 837$ and $\alpha = -0.75$ on 256×256 cells. Each frame shows a domain evolution pattern of 25 % reversal for a sample having the corresponding values of m and w , as denoted in the top and left margins of the domain-pattern arrays, respectively. All the domain evolution patterns systematically change with either changing m or w , and one can clearly find three peculiar domain patterns: i) a large domain, ii) dendrite-like stripe domains, and iii) small nucleated domains. It should be pointed out that the fundamental characteristics of these domain evolution patterns are

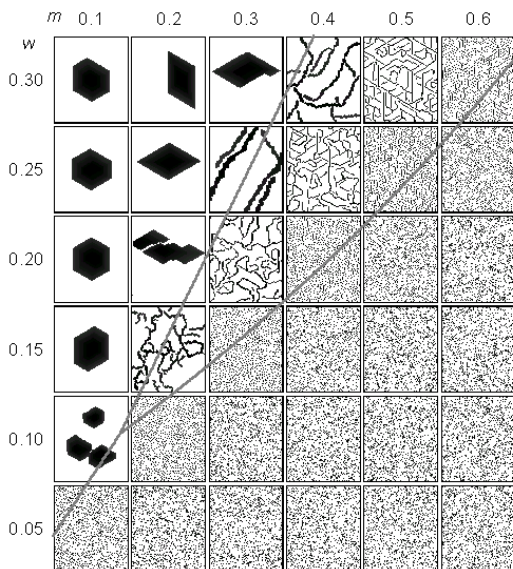


Fig. 16. Simulated domain evolution patterns with respect to the magnetostatic energy m and the domain-wall energy w . Each frame is aligned in a column with m and in a row with w , which shows the domain evolution pattern of 25 % reversal for a sample having the corresponding value of m and w , as denoted in the top and the left margins of the array, respectively. The gray lines show the phase equilibrium lines determined by Eq. (13).

basically unchanged, irrespective of the elapsed time (or the reversal percentage); thus, they can be considered as invariant features closely related to the quasi-ground energy state of the static domain patterns. We plot the phase equilibrium lines together with the simulated domain evolution patterns as seen by the gray lines in the figure. It is clear that the domain evolution patterns are well classified by the phase diagram: all the domain evolution patterns of each extreme phase appear inside the corresponding partition whereas the intermediate patterns are seen around the phase equilibrium lines. It is worthwhile to note that these contrasting patterns are truly consistent with the experimental domain observations in Fig. 6. Thus, one can conclude that contrasting domain reversal dynamics is mainly ascribed to the difference in the macroscopic magnetic properties.

VII. LOCAL MAGNETIC VARIATION

1. Experimental Probing

To verify the effect of the local magnetic variation in ferromagnetic thin films, we have examined the domain reversal behavior among the Co/Pd multilayer samples with varying numbers of repeats, where the macroscopic magnetic properties of these samples were confirmed to be basically the same from measurements of the satura-

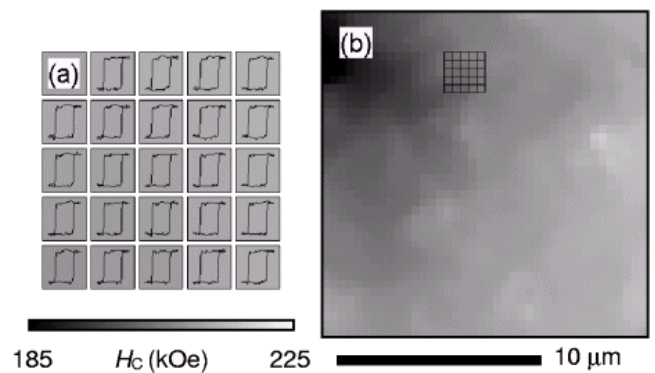


Fig. 17. (a) Typical hysteresis loops measured from each corresponding local region of $400 \times 400 \text{ nm}^2$ on a $(2.5\text{-}\text{\AA} \text{ Co}/11\text{-}\text{\AA} \text{ Pd})_5$ sample, where the x -axis is in the direction of the applied field ranging from -0.4 to 0.4 kOe and the y -axis is the normalized Kerr angle. (b) Distribution map of the local coercivity generated from the simultaneous probing of the local hysteresis loops.

tion magnetization and of the magnetic anisotropy using a vibrating sample magnetometer and a torque magnetometer, respectively. However, the domain reversal behavior was found to change sensitively from wall-motion dominant to nucleation-dominant behavior with increasing number of repeats, as seen in Fig. 6.

To understand this phenomenon, we used the MOMEM system to investigate the local magnetic variation via probing the local coercivity distribution [32]. Using the MOMEM, we could, indeed, probe the variation of the local hysteresis variation of the $(2.5\text{-}\text{\AA} \text{ Co}/11\text{-}\text{\AA} \text{ Pd})_5$ sample, as demonstrated in Fig. 17. The typical hysteresis loops of a small portion of the sample area are illustrated in Fig. 17(a), where each loop shows the local hysteresis loop of a corresponding unit area of $400 \times 400 \text{ nm}^2$. The shapes of the hysteresis loops appear to be same, but a close examination reveals that the value of the coercivity varies slightly. We generated a coercivity distribution map from the local hysteresis loops by mapping the corresponding grays for each coercivity H_C onto the 2-dimensional XY plane, as shown in Fig. 17(b). The figure vividly shows the spatial fluctuation of the local coercivity on a submicrometer scale; the local areas having the lowest coercivity, indicated by black, are nucleation sites in the magnetization reversal process, as will be seen later.

The local dynamic behavior during magnetization reversal under a constant magnetic field was also investigated by means of the MOMEM system [32]. The typical magnetization viscosity curves [36,37] are illustrated in Fig. 18(a), where each curve shows the local viscosity of a corresponding unit area of $400 \times 400 \text{ nm}^2$. Each curve was an average of 16 sequential measurements to reduce the error from the statistical reversal probability. In each curve, the x -axis is the elapsed time on a logarithmic scale with a range from 0.2 to 20 sec from the application of the reversing magnetic field, and the y -axis is the

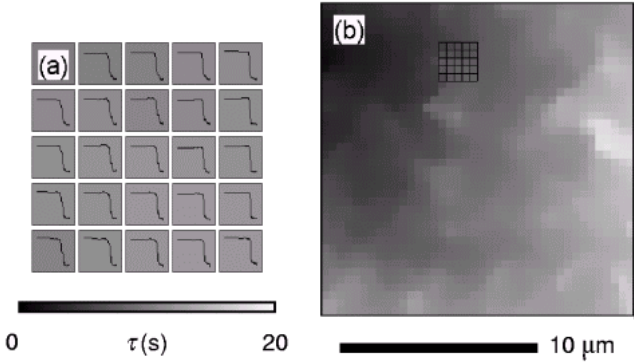


Fig. 18. (a) Typical viscosity curves measured from each corresponding local region shown in Fig. 17, where the x -axis is the elapsed time on a logarithmic scale with a range from 0.2 to 20 s and the y -axis is the normalized Kerr angle. The curves were obtained under a constant magnetic field of 196 Oe, which corresponded to an approximately 90 % mean coercivity. (b) Distribution map of the local switching time generated from the simultaneous probing of the local viscosity curves.

normalized Kerr signal. It is clearly seen in the curves that the magnetization viscosity curves change on a submicrometer scale. The switching time τ was determined from each corresponding curve, and the magnitude of the switching time was indicated by filling the corresponding grays on each pixel according to the gray palette at the bottom of the figure. Therefore, using the MOMM, we could also generate the spatial distribution map of the local switching time on a submicrometer scale from the viscosity curve measurement, as illustrated in Fig. 18(b). The switching time distribution shown in this figure is equivalent to the time-resolved domain evolution patterns shown in Fig. 6. The figure clearly shows that the local switching time is also nonuniform on a submicrometer scale. The domain reversal dynamics of this sample is dominated by the wall-motion process from several nucleation sites located at the isolated black spots, indicating a faster switching time. The smooth variation of the reversal-time distribution indicates a gradual expansion of domains via a continuous wall-motion process from the nucleation sites. The non-isotropic domain reversal behavior implies spatial inhomogeneity in the magnetic properties, possibly caused by structural and/or chemical variation [40].

An important dynamic quantity could be obtained from the magnetic field dependence of the switching time [33]. We measured an array of the field dependencies of the local regions by tracing the switching time at every corresponding pixel under various applied magnetic fields. The field dependency of the switching time is illustrated in each box of Fig. 19(a), where the x -axis is the applied magnetic field on a linear scale, and the y -axis is the switching time on a logarithmic scale. We clearly see from each box that the switching time depends exponentially on the applied magnetic field. The

exponential dependency can be analyzed within the context of a thermally activated relaxation process:

$$\tau = \tau_0 \exp(M_S V_A (H_C - h) / k_B T), \quad (14)$$

where τ_0 is the characteristic switching time for the coercivity H_C . The equation is derived from the Néel-Brown model [41,42] by assuming a first-order uniaxial anisotropy and by using a linear expansion of the energy barrier with h near the mean coercivity. The clear exponential dependency for every local region directly demonstrates that a thermally activated magnetization reversal process takes place, respectively, at the local regions on a submicrometer scale in ferromagnetic thin films. It is worthwhile to mention that we could determine the activation magnetic moment $m_A (=M_S V_A)$ from the best fit using Eq. (14). The activation magnetic moment basically characterizes the basic magnetic moment acting as a single magnetic particle during magnetization reversal, but the physical interpretation of the activation magnetic moment is rather complicated since it is not only ascribed to the intrinsic local nature but also affected by the interaction with the magnetization states of neighbor regions. However, it was confirmed that the activation magnetic moment was inherently reproducible on any local regions in a given sample. Figure 19(b) shows the local variation map of the activation magnetic moment.

In Table 1, we list the local distribution of the magnetic properties in the $(2.5\text{-}\text{\AA} \text{ Co}/11\text{-}\text{\AA} \text{ Pd})_n$ samples with different n . It is surprising to note that the local coercivity distribution sensitively depends on the number of repeats: the thinner film with $n = 5$ shows a smooth variation of the local coercivity while the thicker film shows a large fluctuation of the local coercivity. The large fluctuation of the local coercivity of the thicker film is possibly ascribed to a larger structural irregularity because local structural irregularities, such as atomic

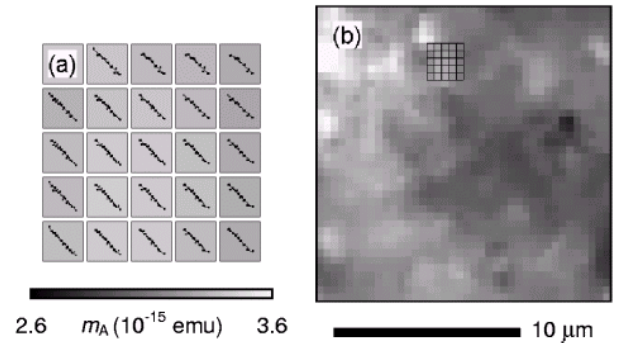


Fig. 19. (a) Typical field dependency measured from each corresponding local region shown in Fig. 17, where the x -axis is in the direction of the applied field ranging from 150 to 200 Oe and the y -axis is the switching time on a logarithmic scale ranging from 1 to 100 s. The solid line in each box represents the best fit using Eq. (13). (b) Distribution map of the local activation magnetic moment generated from the simultaneous probing of the local field dependency.

Table 1. Local distribution of the magnetic properties in $(2.5\text{-}\text{\AA}\text{ Co}/11\text{-}\text{\AA}\text{ Pd})_n$ samples with different n .

n	H_C (Oe)	m_A (10^{-15} emu)
5	149 ± 6	3.7 ± 0.4
10	638 ± 19	
15	916 ± 45	1.6 ± 0.9

misfits, defects, and dislocations, may be accumulative during the film deposition. Local structural irregularity is known to cause magnetic inhomogeneity such as misorientation of the polycrystalline axis, reduction of the nucleation field, and domain-wall pinning.

It is very interesting to note that the reversal pattern in Fig. 18 coincides with the local coercivity distribution for the corresponding sample area shown in Fig. 17. The reversal mechanism under the local coercivity variation can be analyzed based on the thermally activated relaxation process. By considering the local coercivity distribution $H_C(x, y)$, we can modify Eq. (14) to a spatially nonuniform function of $\tau(x, y)$ as given by

$$\tau(x, y) = \tau_0 \exp(M_S V_A (H_C(x, y) - h) / k_B T). \quad (15)$$

Since the magnetization reversal primarily happens in regions of faster $\tau(x, y)$ while the reversal process is impeded at regions of slower $\tau(x, y)$, the domain reversal pattern is sensitive to the local switching time variation. As the local coercivity variation is increased, the wall-motion is pinned at regions of slower reversal speed; then, reversal proceeds by nucleation at regions of faster reversal speed, irrespectively of existing domains. This type of reversal behavior is empirically perceived as a nucleation-dominant reversal. On the other hand, the reversal behavior under a smooth coercivity distribution is dominated by the wall motion overcoming the smaller wall-pinning effect.

The correlation between τ and H_C was, indeed, probed by a quantitative analysis technique using the Momm system [32]. For a quantitative analysis of the correlation, we have measured the number of pixels $N(H_C, t)$ obtained by counting the pixels having the corresponding values of $H_C(x, y)$ and $\tau(x, y)$ measured at the same (x, y) th pixel in the map. Figure 20(a) illustrates the correlated distribution of $N(H_C, \tau)$ on a logarithmic scale in the $H_C - \tau$ coordinate. In the figure, we clearly see that the local switching time is truly correlated with the coercivity distribution. The correlated distribution is rather diffused since reversal dynamics is a statistical phenomena based on the reversal probability. It was experimentally confirmed that by averaging over a larger number of observations, the reversal pattern approached a certain statistical ensemble. The correlation could be analyzed within the context of a thermally activated relaxation process. The solid line in Fig. 20(a) exhibits the best fit of the correlated distribution by a fitting function with an exponential dependence in the thermally activated

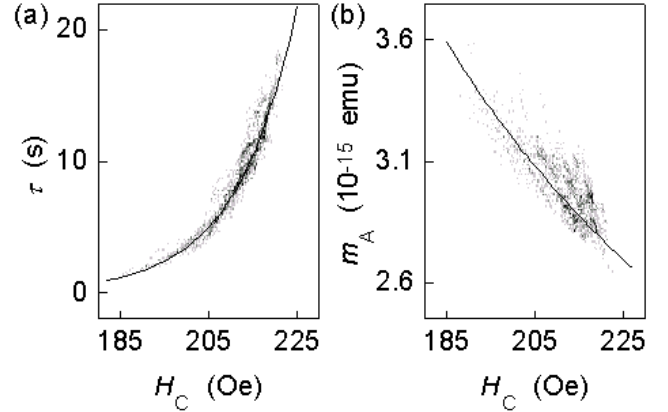


Fig. 20. (a) Correlated distribution between the coercivity H_C in Fig. 17 and the switching time τ in Fig. 18. The solid line represents the best fit using Eq. (13). (b) Correlated distribution between the coercivity H_C in Fig. 17 and activation magnetic moment m_A in Fig. 19. The solid line shows an inverse proportionality.

relaxation process, as given by Eq. (15). The excellent theoretical correlation fitting with the experimental data provides strong evidence that magnetization reversal in ferromagnetic thin films can be described by a thermally activated reversal process based on the local coercivity variation on a submicrometer scale [32–34].

We also see a correlation between the activation magnetic moment and the coercivity. In Fig. 20(b), we illustrate the correlated distribution in the $H_C - m_A$ coordinate. The figure shows that the activation magnetic moment inversely correlates with the coercivity, as shown by a solid line of the best fit. The inverse proportionality possibly comes from the contribution of the anisotropy field, which is known to be inversely proportional to the magnetization.

2. Micromagnetic Simulation

To clarify the influence of the local magnetic variation on the domain reversal behavior, we carry out another simulation based on the Monte Carlo algorithm described in Sec. VI. In this simulation, we give the local fluctuation in the magnitude of the uniaxial magnetic anisotropy to induce the local irregularity of a sample [25,27]. The anisotropy distribution $K_U(x, y)$ is chosen to be spatially non-correlated, and to have a Gaussian distribution in magnitude with the standard deviation δ :

$$K_U(x, y) = \bar{K}_U (1 + \delta f(x, y)), \quad (16)$$

where \bar{K}_U is the mean value of the anisotropy and $f(x, y)$ is a spatially non-correlated fluctuating function having a unit standard deviation. In the simulation, the same function $f(x, y)$ and the same magnetic properties are

Table 2. Magnetic parameters used in the simulation.

Magnetic parameters	Values
Uniaxial anisotropy K_u	1×10^6 erg/cm ³
Saturation magnetization M_s	250 emu/cm ³
Wall energy density σ_w	0.8 erg/cm ²
Unit cell volume V_c	6.93×10^{-18} cm ³
Cell distance d_c	20 μ m
Film thickness t_f	20 μ m

The values were chosen from the typical magnetic properties of Co/Pd multilayers [5,13]

used, except the magnitude of fluctuation δ is varied. The magnetic parameters in the simulation are chosen as typical values of the magnetic properties in Co/Pd nanomultilayered system, as listed in Table 2.

Interestingly, magnetization reversal behavior is very sensitive to the degree of the fluctuation in anisotropy. Figure 21 shows the simulated domain patterns of magnetic thin films having a uniaxial anisotropy fluctuation δ of (a) 0, (b) 2, and (c) 4 %, respectively. The figures were grabbed at 10, 30, and 50 % reversal as denoted at the top of each column, respectively, and the black regions in the figures illustrate the reversed domain patterns from the saturated state.

From the figures, one can vividly observe the contrasting domain reversal behaviors among the samples. Wall-

motion dominant reversal is clearly seen from Fig. 21(a). In this sample, the domain is hardly nucleated. However, once nucleated, domains expand gradually in size at all domain boundaries due to wall motion. Finally, a large regular domain is clearly observed. On the other hand, nucleation-dominant reversal is vividly observed in Fig. 21(c). In this system, the nucleation occurs at a number of places, but the nucleated domain grow only marginally in size. The domain expands anisotropically by means of the nucleation adjacent to the existing domain boundaries. Then, the dendrite-like domains are formed throughout the entire area of the sample. An intermediate reversal behavior mixed with domain-wall expansion and random nucleation is seen in Fig. 21(b). The domain reverses due to not only growth of random jutting-out nucleation but also areal expansion of the domain wall in every domain boundary. Thus, ragged domains rather than a single regular domain are formed, and the domains are larger in size than those in Fig. 21(c).

It is interesting to point out that these contrasting domain patterns result from an anisotropy fluctuation of only a few percent. This degree of anisotropy fluctuation is often observed in real films due to structural irregularities generated during the vacuum deposition since the anisotropy is a structure-sensitive magnetic property [14, 40]. Note that the contrasting domain patterns shown in Fig. 21 are truly matched to the experimentally observed domain reversal behaviors between wall-motion dominant reversal and nucleation-dominant reversal, as shown in Fig. 6. These results demonstrate the crucial influence of the non-uniformity in the magnetic properties on the reversal process. Thus, by considering structural non-uniformity, including film thickness, underlayers, substrates, deposition techniques, and so on, one can explain the contrasting reversal behaviors among the same compositional samples prepared by different preparation conditions.

Based on these simulation results, together with the simulation results shown in Sec. V, one can conclude that the reversal behavior in real films is determined by both the local magnetic variation and the macroscopic magnetic properties, but it is not easy to distinguish the difference between these two.

VIII. CONCLUSIONS

We have developed a magneto-optical microscope magnetometer (MOMM) capable of real-time grabbing domain reversal patterns under an applied external magnetic field, and of simultaneously probing the local magnetic properties with a 400-nm spatial resolution. Using the MOMM system, we have investigated the domain reversal dynamics in Co/Pd multilayer samples: the domain reversal dynamics sensitively changes from wall-motion-dominant to nucleation-dominant reversal either

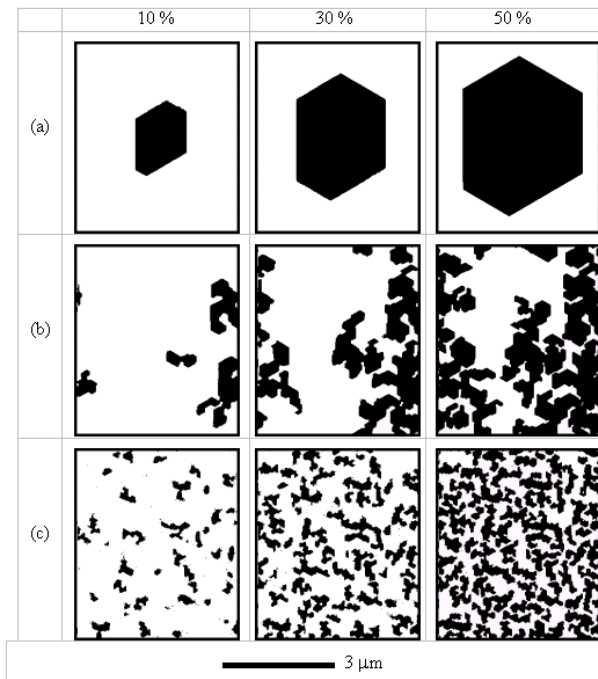


Fig. 21. Simulated domain patterns of the samples having an anisotropy variation of (a) 0, (b) 2, and (c) 4 %. The numbers denoted at the top of each column are the areal fractions of the reversed domain.

with increasing number of repeats or with increasing Co-sublayer thickness of the Co/Pd multilayer. From a quantitative analysis, the reversal ratio of the wall-motion speed over the nucleation rate is the governing parameter for the contrasting domain reversal dynamics. The activation volumes of the wall-motion and nucleation processes are found to be unequal, and the difference is closely related with the domain dynamics. Based on a Monte-Carlo simulation, both the macroscopic magnetic properties and the local magnetic variation are responsible for the contrasting domain reversal behavior.

ACKNOWLEDGMENTS

This work was supported by the Korean Ministry of Science and Technology through the Creative Research Initiative Project. We thank Yoon-Chul Cho, Hyuk-Jae Jang, and Kwang-Su Ryu for their experimental assistances.

REFERENCES

- [1] J. Pommier, P. Meyer, G. Pónissard, J. Ferré, P. Bruno and D. Renard, *Phys. Rev. Lett.* **65**, 2054 (1990).
- [2] J. Ferré, J. P. Jamet and P. Meyer, *Phys. Stat. Sol. (a)* **175**, 213 (1999).
- [3] A. Kirilyuk, J. Ferré, V. Grolier, J. P. Jamet and D. Renard, *J. Magn. Magn. Mater.* **171**, 45 (1997).
- [4] B. Raquet, R. Mamy and J. C. Ousset, *Phys. Rev. B* **54**, 4128 (1996).
- [5] S.-B. Choe and S.-C. Shin, *Phys. Rev. B* **57**, 1085 (1998); *J. Appl. Phys.* **81**, 5743 (1997).
- [6] S.-B. Choe and S.-C. Shin, *Phys. Rev. B* **59**, 142 (1999); *J. Magn. Magn. Mater.* **198-199**, 474 (1999).
- [7] S.-B. Choe and S.-C. Shin, *Appl. Phys. Lett.* **70**, 3612 (1997); *J. Appl. Phys.* **83**, 6952 (1998).
- [8] H.-P. D. Shieh and M. H. Kryder, *IEEE Trans. Magn.* **24**, 2464 (1988).
- [9] R. P. Cowburn, D. K. Koltsov, A. O. Adeyeye and M. E. Welland, *Appl. Phys. Lett.* **73**, 3947 (1998); *Phys. Rev. Lett.* **81**, 5414 (1998).
- [10] T. Aign, P. Meyer, S. Lemerle, J. P. Jamet, J. Ferré, V. Mathet, C. Chappert, J. Gierak, C. Vieu, F. Rousseaux, H. Launios and H. Bernas, *Phys. Rev. Lett.* **81**, 5656 (1998).
- [11] J.-P. Jamet, S. Lemerle, P. Meyer, J. Ferré, B. Bartelien, N. Bardou, C. Chappert, P. Veiller, F. Rousseaux, D. Decanini and H. Launois, *Phys. Rev. B* **57**, 14320 (1998).
- [12] J. X. Shen, R. D. Kirby, Z. S. Shan, D. J. Sellmyer and T. Suzuki, *J. Appl. Phys.* **73**, 6418 (1993).
- [13] S.-C. Shin and S.-B. Choe, *IEEE Trans. Magn.* **35**, 3853 (1999); *J. Appl. Phys.* **85**, 5651 (1999).
- [14] S.-B. Choe, H.-J. Jang and S.-C. Shin, *IEEE Trans. Magn.* **35**, 3892 (1999); *J. Magn. Magn. Mater.* **209**, 84 (2000).
- [15] S.-B. Choe and S.-C. Shin, *J. Magn. Magn. Mater.* **236**, 249 (2001).
- [16] E. Dan Dahlberg and J.-G. Zhu, *Phys. Today* **48**, 34 (1995).
- [17] E. Betzig, J. K. Trautman, R. Wolfe, E. M. Gyorgy, P. L. Finn, M. H. Kryder and C. H. Chang, *Appl. Phys. Lett.* **61**, 142 (1992).
- [18] M. R. Scheinfein, J. Unguris, M. H. Kelley, D. T. Pierce and R. J. Celotta, *Rev. Sci. Instrum.* **61**, 2501 (1990).
- [19] R. Wiesendanger, H.-J. Güntherodt, G. Güntherodt, R. J. Gambino and R. Ruf, *Phys. Rev. Lett.* **65**, 247 (1990).
- [20] H. Poppa, E. Bauer and H. Pinkvos, *MRS Bull.* **20**, 38 (1995).
- [21] S. Anders, H. A. Padmore, R. M. Duarte, T. Renner, M. R. Scheinfein, J. Stöhr, L. Séve and B. Sinkovic, *Rev. Sci. Instr.* **70**, 3973 (1999).
- [22] P. Fischer, T. Eimüller, G. Schütz, P. Guttmann, G. Schmahl, K. Prügl and G. Bayreuther, *J. Phys. D* **31**, 649 (1998).
- [23] M. Mansuripur, *The Physical Principles of Magneto-Optical Recording* (Cambridge University Press, Cambridge, 1995), Chap. 15; *J. Appl. Phys.* **66**, 3731 (1989); *J. Appl. Phys.* **61**, 1580 (1987).
- [24] R. D. Kirby, J. X. Shen, R. J. Hardy and D. J. Sellmyer, *Phys. Rev. B* **49**, 10810 (1994).
- [25] A. Lyberatos, J. Earl and R. W. Chantrell, *Phys. Rev. B* **53**, 5493 (1996); *J. Magn. Magn. Mater.* **186**, 248 (1998); *J. Phys. D* **33**, R117 (2000).
- [26] U. Nowak, J. Heimele, T. Kleinfeld and D. Weller, *Phys. Rev. B* **56**, 8143 (1997).
- [27] S.-B. Choe and S.-C. Shin, *IEEE Trans. Magn.* **36**, 3167 (2000); *J. Korean Phys. Soc.* **39**, 359 (2001).
- [28] A. Moschel, R. A. Hyman and A. Zangwill, *Phys. Rev. Lett.* **77**, 3653 (1996).
- [29] M. Speckmann, H. P. Oepen and H. Ibach, *Phys. Rev. Lett.* **75**, 2035 (1995).
- [30] J. Ferré, V. Grolier, P. Meyer, S. Lemerle, A. Maziewski, E. Stefanowicz, S. V. Tarasenko, V. V. Tarasenko, M. Kisielewski and D. Renard, *Phys. Rev. B* **55**, 15092 (1997).
- [31] H. Hopster, *Phys. Rev. Lett.* **83**, 1227 (1999).
- [32] S.-B. Choe and S.-C. Shin, *Phys. Rev. B* **62**, 8646 (2000); *J. Appl. Phys.* **87**, 6848 (2000); *J. Appl. Phys.* **88**, 3096 (2000).
- [33] S.-B. Choe and S.-C. Shin, *Appl. Phys. Lett.* **78**, 1430 (2001); *J. Appl. Phys.* **89**, 7227 (2001).
- [34] S.-B. Choe and S.-C. Shin, *Phys. Rev. Lett.* **86**, 532 (2001); *J. Appl. Phys.* **87**, 5076 (2000); *J. Appl. Phys.* **90**, 1419 (2001).
- [35] S.-B. Choe and S.-C. Shin, *J. Magn. Magn. Mater.* **221**, 255 (2000); *J. Korean Phys. Soc.* **38**, 392 (2001).
- [36] M. Labrune, S. Andrieu, F. Rio and P. Bernstein, *J. Magn. Magn. Mater.* **80**, 211 (1989).
- [37] E. Fatuzzo, *Phys. Rev.* **127**, 1999 (1962).
- [38] R. W. Chantrell, *J. Magn. Magn. Mater.* **95**, 365 (1991); T. Thomson, K. O'Grady and R. W. Chantrell, *IEEE Trans. Magn.* **28**, 2518 (1992).
- [39] W. Wernsdorfer, E. B. Orozco, K. Hasselbach, A. Benoit, B. Barbara, N. Demoncy, A. Loiseau, H. Pascard and D. Mailly, *Phys. Rev. Lett.* **78**, 1791 (1997).
- [40] H. Kronmüller, *Phys. Stat. Sol. (b)* **144**, 385 (1987).
- [41] L. Néel, *Ann. Geophys.* **5**, 99 (1949).
- [42] W. F. Brown, *Phys. Rev.* **130**, 1677 (1963).